Development/Plasticity/Repair

Extensive Structural Remodeling of the Axonal Arbors of Parvalbumin Basket Cells during Development in Mouse Neocortex

Kristina D. Micheva,* Marianna Kiraly,* Marc M. Perez, and Daniel V. Madison
Department of Molecular and Cellular Physiology, Stanford University, Stanford, California 94305

Parvalbumin-containing (PV^+) basket cells are specialized cortical interneurons that regulate the activity of local neuronal circuits with high temporal precision and reliability. To understand how the PV^+ interneuron connectivity underlying these functional properties is established during development, we used array tomography to map pairs of synaptically connected PV^+ interneurons and postsynaptic neurons from the neocortex of mice of both sexes. We focused on the axon-myelin unit of the PV^+ interneuron and quantified the number of synapses onto the postsynaptic neuron, length of connecting axonal paths, and their myelination at different time points between 2 weeks and 7 months of age. We find that myelination of the proximal axon occurs very rapidly during the third and, to a lesser extent, fourth postnatal weeks. The number of synaptic contacts made by the PV^+ interneuron on its postsynaptic partner meanwhile is significantly reduced to about one-third by the end of the first postnatal month. The number of autapses, the synapses that PV^+ interneurons form on themselves, however, remains constant throughout the examined period. Axon reorganizations continue beyond postnatal month 2, with the postsynaptic targets of PV^+ interneurons gradually shifting to more proximal locations, and the length of axonal paths and their myelin becoming conspicuously uniform per connection. These continued microcircuit refinements likely provide the structural substrate for the robust inhibitory effects and fine temporal precision of adult PV^+ basket cells.

Key words: **array tomography; connection mapping; interneuron; myelin; neocortex**

Significance Statement

The axon of adult parvalbumin-containing (PV^+) interneurons is highly specialized for fast and reliable neurotransmission. It is myelinated and forms synapses mostly onto the cell bodies and proximal dendrites of postsynaptic neurons for maximal impact. In this study, we follow the development of the PV^+ interneuron axon, its myelination and synapse formation, revealing a rapid sequence of axonal reorganization, myelination of the PV^+ interneuron proximal axon, and pruning of almost two-thirds of the synapses in an individual connection. This is followed by a prolonged period of axon refinement and additional myelination leading to a remarkable precision of connections in the adult mouse cortex, consistent with the temporal precision and fidelity of PV^+ interneuron action.

Introduction

Parvalbumin-positive (PV^+) basket cells are the most abundant type of inhibitory interneurons in neocortex. Found in all cortical layers, except layer 1, and in all cortical areas (Rudy et al., 2011), they form synapses onto hundreds of neighboring pyramidal neurons and interneurons (Packer and Yuste et al., 2011) targeting preferentially their cell bodies and proximal dendrites (Somogyi et al., 1983; Tamás et al., 1997a; Kawaguchi and Kubota, 1998). This connectivity underlies the many important roles of PV^+ basket cells, such as controlling cortical rhythmic activity (Cardin et al., 2009; Buzsáki and Wang, 2012; Cardin, 2018; Chariker et al., 2018), regulating the excitatory/inhibitory balance (Xue et al., 2014; Ferguson and Gao, 2018), and controlling spike timing of pyramidal neurons (Pouille and Scanziani, 2001; Wehr and Zador, 2003). The initial connectivity of PV^+

Received Apr. 23, 2021; revised Sep. 12, 2021; accepted Sep. 21, 2021.

Author contributions: K.D.M., M.K., and D.V.M. designed research; K.D.M., M.K., M.M.P., and D.V.M. analyzed data; K.D.M. and D.V.M. edited the paper; K.D.M. wrote the paper; M.K. and M.M.P. performed research.

This work was supported by National Institutes of Health NS094499 to D.V.M.; the Harold and Leila Y. Mathers Charitable Foundation; and the Discovery Innovation Fund in Basic Biomedical Sciences from Stanford University.

*K.D.M. and M.K. contributed equally to this work and are joint first authors.

K.D.M. has founder's equity interests in Aratome, LLC (Menlo Park, CA), an enterprise that produces array tomography materials and services. The remaining authors declare no competing financial interests.

Correspondence should be addressed to Kristina D. Micheva at kmicheva@stanford.edu or Daniel V. Madison at madison@stanford.edu.

https://doi.org/10.1523/JNEUROSCI.0871-21.2021
Copyright © 2021 the authors

interneurons is established rapidly during the early postnatal ages, followed by circuit refinement that underlies learning and plasticity and continues through adult life. During the first postnatal week in mouse neocortex, the majority of PV^+ interneurons migrate to their final laminar destination and form synapses with neighboring neurons (Lim et al., 2018). Then, toward the end of this first week, many PV^+ interneurons begin to die off, and by P10 as many as 40% of the PV^+ interneurons, thought to be the ones that did not successfully integrate in the developing neuronal circuits (Southwell et al., 2012; Wong et al., 2018), undergo apoptosis. Around the same time, profound changes are seen in the expression of numerous genes in PV^+ interneurons, including genes involved in synaptic function (Okaty et al., 2009). PV^+ expression appears around P12-P14 (del Río et al., 1994). Electrophysiological properties of PV^+ interneurons also change dramatically, including the loss of spike-frequency adaptation between P10 and P15 and large increase in the maximum firing rate (Okaty et al., 2009; Miyamae et al., 2017). Thus, within the span of <2 weeks, neocortical PV^+ basket cells arrive at their final destination, establish synaptic connections, and integrate into the developing neocortical circuit or perish.

While the genetic programs and molecular mechanisms of this initial development of neocortical PV^+ interneurons have been extensively characterized (Lim et al., 2018), much less is known about the synaptic connectivity of the surviving PV^+ interneurons at this stage and the subsequent reorganization of their axonal arbors during circuit refinement. During the second half of the first postnatal month, the number of the perisomatic synapses that PV^+ interneurons form around nearby pyramidal neurons gradually increases (Chattopadhyaya et al., 2004). This is the net result of ongoing new synapse formation and synapse elimination, in an activity-dependent manner (Chattopadhyaya et al., 2004; Wu et al., 2012). At the same time, as these interneurons mature, their proximal axonal arbor becomes myelinated in a characteristic patchy manner (Zonouzi et al., 2019). How do these events unfold relative to one another? When does the myelination take place? How do myelination and synaptic formation/pruning reshape the axonal arbor? These are the questions that our current study addresses. Using array tomography (AT), we map the connectivity in pairs of synaptically connected PV^+ interneurons and postsynaptic neurons and quantify the number of synapses, length of connecting axonal paths, and their myelination at different time points between 2 weeks of age and 7 months. We find that myelination of the proximal axon occurs very rapidly during the second half of the first postnatal month. Massive synapse pruning takes place in the fourth postnatal week and results in about threefold reduction of synaptic contacts made by the PV^+ interneuron on its postsynaptic partner. In contrast, the number of autapses, the synapses that the PV^+ interneuron makes on itself, remains constant throughout this time. Our study reveals the extensive reorganization of the PV^+ interneuron axonal arbor and synapses, resulting in the remarkably precise adult connectivity pattern characterized by synapses proximal to the postsynaptic cell body and a uniform length of axonal paths to these synapses.

Materials and Methods

Animals. Young mice C57BL/6 of both sexes, ages P14 and P22, were used for this study. All procedures related to the care and treatment of animals were conducted in accordance with the *Guide for the care and use of laboratory animals* of the National Institutes of Health and approved by the Administrative Panel on Laboratory Animal Care at Stanford University. To study the developmental sequence, we also analyzed data from additional 14 pairs at ages spanning up to 7 months (1 pair at P22, 4 pairs at 1 month, 5 pairs at 2 months, and 4 pairs at 7 months) used in a previous study (Micheva et al., 2021).

Preparation of acute neocortical slices. Brain slices were prepared exactly following the protocol of Ting et al. (2018). Briefly, mouse brains were hemisected, embedded in 2% agarose, and cut to a thickness of 300 μm using a Compresstome vibrating microtome (Precisionary Instruments). Slices were stored submerged for at least 1 h at room temperature in a Model 4 Brain Slice Keeper (AutoMate Scientific). During this incubation period, slices were subjected to the Wisteria floribunda lectin staining procedure below. For recording, slices were transferred to a submerged/superfusing slice chamber with a glass coverslip bottom (Warner Instruments) on the stage of an upright microscope.

PV^+ interneuron identification. To identify PV^+ interneurons in living tissue, the perineuronal nets that selectively surround these neurons were stained in the live slices using fluorescein-labeled W. floribunda lectin (Vector Labs, FL-1351), following the protocol of Hoppenrath et al. (2016). Briefly, immediately after sectioning on the Compresstome, slices were transferred into a small volume of holding buffer (in mM as follows: 92 NaCl, 2.5 KCl, 1.25 NaH_2PO_4, 30 $NaHCO_3$, 20 HEPES, 25 glucose, 2 thiourea, 5 Na-ascorbate, 3 Na-pyruvate, 2 $CaCl_2{\cdot}2H_2O$, and 2 $MgSO_4{\cdot}7H_2O$, pH 7.3-7.4) containing fluorescein-labeled W. floribunda lectin (20 μg/ml) and maintained at room temperature under a 95% O_2, 5% CO_2 atmosphere for 1 h. Labeled perineuronal nets were detected in the live slices using epifluorescence (Nikon GFP filter cube). The identity of the neurons labeled by the W. floribunda lectin was previously confirmed by us using subsequent immunofluorescent labeling with anti-PV antibody (Micheva et al., 2021).

Electrophysiology. We performed simultaneous whole-cell recordings from two different neurons from the mouse medial temporal lobe (perirhinal and entorhinal cortex). The presynaptic PV^+ basket cell was identified by W. floribunda labeling of its perineuronal net (Hoppenrath et al., 2016), and a nearby postsynaptic pyramidal neuron was chosen by its shape. Neurons at a 30-50 μm depth were targeted because healthy neurons were typically located below 30 μm of depth within the slice (Ting et al., 2018), and W. floribunda labeling was usually limited within the surface 50 μm. The presynaptic interneuron was recorded in current clamp, and the postsynaptic neuron in single-electrode continuous voltage clamp (Molecular Devices Multiclamp 700A). Single-action potentials were elicited from the presynaptic interneuron by the injection of positive current through the recording electrode, with the amplitude and duration of the current pulse adjusted to produce a single action potential. Data were sampled at 10 kHz and low pass filtered between 3 and 10 kHz. The postsynaptic recording was examined for time-locked postsynaptic responses to that presynaptic action potential. Typically, at least 25 action potentials/IPSC trials were recorded per cell. We measured the amplitude of the evoked postsynaptic current and the latency of that current, relative in time to the peak of the presynaptic action potential. The detailed methods, including recording configurations, solutions, electrodes, etc., were as described previously (Pavlidis and Madison, 1999; Montgomery et al., 2001), except that the postsynaptic electrode internal solution consisted of the following (in mM): 120 KCl, 40 HEPES, 2 Mg-ATP, 0.317 Na-GTP, and 10.7 $MgCl_2$. In addition to making the IPSCs larger and easier to detect, use of high chloride solution also reversed the usual polarity of inhibitory synaptic currents to inward. To mark the neurons for subsequent AT analysis, the presynaptic interneuron internal electrode solution included 0.1% AlexaFluor-594 hydrazide (Thermo Fisher Scientific, A-10 438) and 0.5% Neurobiotin (Vector Laboratories, SP-1120-50), and the postsynaptic neuron internal electrode solution contained 0.2% Lucifer yellow CH, potassium salt (Thermo Fisher Scientific, L1177).

Slice fixation and embedding in resin. After the electrophysiological recordings, the slice was placed in a fixative containing 2% formaldehyde (Electron Microscopy Sciences, 157-8) and 2% glutaraldehyde (Electron Microscopy Sciences, 16220) in PBS, first at room temperature for 1 h, and then at 4°C for 24 h. Slices were subsequently washed in PBS, and a smaller area (~1 by 2 mm) around the labeled neurons was dissected out and dehydrated serially in washes of 50%, 70%, 70% ethanol, at 4°C,

10 min for each step. The dehydrated tissue was then infiltrated with LR White resin, hard grade (Electron Microscopy Sciences, 14383), first with a mixture of 70% ethanol and LR White (1:3) and then in three changes of 100% LR White, 10 min at room temperature each step. The slice was left in unpolymerized LR White resin overnight at 4°C, then transferred to a gelatin capsule size "00" (Electron Microscopy Sciences 70100), and polymerized for 24 h at 55°C. The polymerized blocks with tissue were stored in the dark at room temperature.

Sectioning. The blocks were trimmed around the tissue to the shape of a trapezoid ~1.5 mm wide and 0.5 mm high, and glue (Weldwood Contact Cement diluted with xylene) was applied with a thin paint brush to the leading and trailing edges of the block pyramid. The embedded plastic block was cut on an ultramicrotome (Leica Ultracut EM UC6) into 100-nm-thick serial sections, which were mounted on gelatin-coated coverslips. Typically, 1000-1200 serial sections containing the fixed tissue slice were obtained from each block.

Immunofluorescent AT. Coverslips with sections containing the filled neurons were identified by visual inspection using a 10× objective under the fluorescence microscope, and were processed for standard indirect immunofluorescence, as described by Micheva et al. (2010). Antibodies were obtained from commercial sources and are listed in Table 1. The sections were pretreated with sodium borohydride (1% in TBS, pH 7.6 for 3 min) to reduce nonspecific staining and autofluorescence. After a 20 min wash with TBS, the sections were incubated in 50 mM glycine in TBS for 5 min, followed by blocking solution (0.05% Tween 20 and 0.1% BSA in TBS) for 5 min. The primary antibodies were diluted in blocking solution as specified in Table 1 and were applied overnight at 4°C. After a 15 min wash in TBS, the sections were incubated with AlexaFluor dye-conjugated secondary antibodies, highly cross-adsorbed (Thermo Fisher Scientific), diluted 1:150 in blocking solution for 30 min at room temperature. Neurobiotin was detected using Streptavidin-Alexa-594 (Thermo Fisher Scientific, S11227), diluted at 1:200, and applied together with the secondary antibodies. Finally, sections were washed with TBS for 15 min, rinsed with distilled water, and mounted on glass slides using SlowFade Diamond Antifade Mountant with DAPI (Thermo Fisher Scientific, S36964). After the sections were imaged, the antibodies were eluted using a solution of 0.2 M NaOH and 0.02% SDS, and new antibodies were reapplied on some of the coverslips, as needed. The first round of staining always included anti-LY and Streptavidin-Alexa-594 to visualize the filled neurons and anti-MBP to detect myelin.

Imaging. The immunostained ribbons of sections were imaged on an automated epifluorescence microscope (Zeiss AxioImager Z1) with AxioVision software (Carl Zeiss) using a 63× Plan-Apochromat 1.4 NA oil objective. To define the position list for the automated imaging, a custom Python-based graphical user interface, MosaicPlanner (obtained from https://code.google.com/archive/p/smithlabsoftware/), was used to automatically find corresponding locations across the serial sections. On average, 600 sections per neuron pair were imaged (ranging between 375 and 826 sections), resulting in volumes of ~140 µm × 400 µm × 60 µm centered on the filled neurons. Images from different imaging sessions were registered using a DAPI stain present in the mounting medium. The images from the serial sections were also aligned using the DAPI signal. Both image registration and alignment were performed with the MultiStackReg plugin in FIJI (Schindelin et al., 2012).

Synapse detection and axon tracing. Immunofluorescent AT is a high-resolution imaging method well suited for synapse detection (Micheva et al., 2010; Collman et al., 2015). The axial resolution is determined by the section thickness (100 nm here), and the lateral resolution is at the theoretical diffraction limit (~200 nm) because the ultrathin section is placed directly on the coverslip. A putative synapse between the two filled neurons was identified as a direct apposition between an enlargement in the presynaptic axon and the postsynaptic neuron, which was present on two or more consecutive sections. Such axonal varicosities of basket cells have previously been shown to correspond to synaptic boutons using electron microscopy in adult cats (Tamás et al., 1997a) and GABA-containing synapses in the rodent neocortex already exhibit adult-like ultrastructure by P15 (Micheva and Beaulieu, 1996). Twenty-two putative synapses from three different P14 pairs were subsequently immunostained with synaptic markers to verify whether these criteria were adequate to identify synapses. The expression of synaptic markers was lower at this age compared with older animals (Micheva et al., 2021), and gephyrin immunoreactivity in particular was ambiguous to assess in many cases (12 of 22 contacts) and was therefore not used for this analysis. Of 22 contacts at this age, 20 were synapsin-immunopositive. At P22, of 16 contacts, all were synapsin-immunopositive. To obtain a better estimate of the potential rate of false-positive and false-negative synapse detections using the current criteria, we analyzed stretches of unmyelinated third and higher-order axonal branches of PV^+ interneurons in the youngest animals examined (P14), when synapse detection is generally more challenging. We found that 96% of axonal varicosities (123 of 128) contain synapsin. In addition, synapsin was observed outside axonal varicosities, at a rate of 13 instances per axonal stretch with 100 varicosities. Assuming that the presence of synapsin within the axon indicates a presynaptic bouton, then the false-positive rate is 4% (the axonal varicosities that lack synapsin but were counted as synapses based on the current criteria), and the false-negative rate is 13% (the synapsin accumulations outside of axonal varicosities, which according to the current criteria were not counted as synapses). This false-negative rate is likely an overestimation because, during development, synapsin is known to be transported along the axon to newly emerging synapses (Ahmari et al., 2000); therefore, not all synapsin outside of axonal varicosities is found within synapses.

Table 1. Antibodies

Antigen	Host	Antibody source	Dilution	RRID
Lucifer Yellow	Rabbit	Thermo Fisher Scientific A-5750	1:200	AB_2536190
Myelin basic protein	Chicken	AVES, MBP	1:100	AB_2313550
Synapsin 1/2	Chicken	Synaptic Systems 106006	1:200	AB_2622240
Gephyrin	Mouse	NeuroMab clone L106/83, 75-443	1:100	AB_2636851
Pan-QKI	Mouse	NeuroMab clone N147/6, 73-168	1:2	AB_10671658

For brevity, in the following sections, the putative synaptic contacts in the imaged pairs are referred to as synapses. Using FIJI, axons were traced back from the synapses to the neuronal cell body. Each connection was traced independently by two experts (M.M.P. and K.D.M.), and axonal path trajectories were saved as a set of ROIs. Myelinated internodes were identified using MBP immunofluorescence, which is a reliable measure of myelin as previously verified using correlative immunofluorescence – SEM (Micheva et al., 2016). Axon diameter was estimated as the average of three measurements (beginning, middle, and end of each internode), using the measure function in FIJI. Axon initial segment diameter was also calculated as the average of three measurements along its length. Together, the following morphologic measurements were obtained: total axonal distance to each synapse; length and diameter of axon initial segment; length, diameter, and number of myelinated internodes; length of nodes of Ranvier; and distance of the postsynaptic target from the postsynaptic cell body. The results for each pair were visualized as maps of the PV^+ interneuron axonal arbors (axonograms) and maps of the postsynaptic neuron dendritic arbors with location of the PV^+ synapses (dendrograms, graphical representation inspired by Aliaga Maraver et al., 2018). Because tissue dehydration and embedding with our protocol result in ~23% linear shrinkage, these measurements were adjusted accordingly (Busse and Smith, 2013).

Statistics. Measurements are presented as average ± SD. Statistical significance between ages was determined using one-way ANOVA with *post hoc* Tukey HSD test. Because no statistically significant differences were detected between P14 and P22, and between 2 months and 7 months, these age groups were combined for some of the analyses, and the results are presented alongside the analyses for all the separate age groups. The number of individual slices was used for sample size *n*, with the assumption that neurons from different slices (300 µm each) are positioned far enough apart in the brain and thus belong to different microcircuits (as the great majority of PV^+ interneuron connections are made within the immediate 200 µm radius), and therefore for the present purposes could be considered as independent. Among the slices analyzed by AT, this occurs in the P22 age group, with the four AT-

Table 2. Neuronal pairs analysis

Pair	Age (mo)	No. of sections	Cortical region	Layer	Postsynaptic cell
MK190314-1	0.5	375	Perirhinal	5	Pyramidal
MK190405-1	0.5	480	Perirhinal	5/6	Pyramidal
MK190307-1	0.5	775	Perirhinal	5	Pyramidal
MK190411-3	0.5	619	Entorhinal	4	Pyramidal
MK210204-3	0.5	718	Entorhinal	5	Pyramidal
MK190129-1*a*	0.75	413	Perirhinal	3/4	Pyramidal
MK190129-2	0.75	826	Perirhinal	5	Pyramidal
MK181205-2	0.75	415	Perirhinal	5	Pyramidal
MK181205-1*b*	0.75	598	Entorhinal	5	Interneuron

[a]This pair is from a previous study (Micheva et al., 2021).
[b]Based on its morphologic appearance and the presence of myelinated axon, the postsynaptic interneuron in this pair is likely a PV^+ interneuron.

analyzed slices coming from 2 different animals (2 slices from each). For all other ages, including the mice from the previous study (Micheva et al., 2021), each slice analyzed by AT came from a different animal. The number of slices and number of animals are also indicated in Results. Linear correlations between two variables were done using Pearson's correlation coefficient. To prepare the boxplots, the web application BoxPlotR was used (http://boxplot.tyerslab.com) (Spitzer et al., 2014).

Results

To analyze the developmental changes in connectivity pattern and axonal myelination of PV^+ interneurons, we recorded from 22 synaptically connected pairs of neurons from 13 mice (18 pairs from 10 mice at P14, and 4 pairs from 3 mice at P22). The presynaptic neuron was always a PV^+ interneuron identified by the fluorescent W. floribunda stain of its perineuronal net, and the postsynaptic neuron was an adjacent neuron, in most cases a pyramidal neuron. Eight of these pairs (5 pairs from 5 mice at P14, and 3 pairs from 2 mice at P22) that had bright and complete neuronal fills were further processed for immunofluorescent AT to find the synapses in each connection and map the connecting axonal arbor (Table 2). The results were compared with data from additional 14 pairs at ages spanning up to 7 months (1 pair at P22, 4 pairs at 1 month, 5 pairs at 2 months, and 4 pairs at 7 months; all pairs were from different animals) that were used in a previous study (Micheva et al., 2021). The 4 pairs where the postsynaptic neuron was an interneuron are indicated in the plots with magenta circles (1 pair at P22, 1 at 2 months, and 2 at 7 months).

Profuse synaptic connectivity of PV^+ interneurons at P14, but scarce myelination of their axons

At the youngest age examined, P14, the interneuronal axon branched profusely and formed numerous axonal varicosities (Figs. 1 and 2). These varicosities were densely distributed on third- and higher-order branches at an average of 3.8 ± 0.6 varicosities per 10 µm of axonal length (average ± SD), and the great majority of them (96%, 122 of 127 axonal varicosities) were immunopositive for synapsin. In individual neuronal pairs, the PV^+ interneuron formed on average 22 ± 8 synapses onto the postsynaptic neuron. This is about twice as many synapses as found in older pairs (9 ± 5 synapses in pairs between 1 and 7 months) (Micheva et al., 2021). Similarly to adult PV^+ interneurons, the synapses were preferentially distributed close to the postsynaptic soma, with an average distance of 35 ± 27 µm from the soma, although a few synapses were seen as far away as 100 µm and further. In addition to the soma, synapses were formed both on the basal and apical dendrites, and, in several occasions (3 of 107), on the axon initial segment. It was not always possible to reliably distinguish between a synapse on a dendritic shaft or spine, or on both shaft and spine as seen with electron microscopy (Somogyi et al., 1983); therefore, we did not include these categories in the analysis, although our best judgment of the postsynaptic target is indicated on the axonograms in Extended Data Fig. 3-1. In each neuronal pair, the PV^+ interneuron synapsed onto multiple postsynaptic domains (5 ± 2) of the postsynaptic neuron via multiple axonal paths (8 ± 2). A neuronal domain was defined as either the cell body or a primary dendrite with its branches. In cases were the primary dendrite branched into two large branches close to the cell body (within 20 µm), these two branches were considered as separate domains. Axonal paths were considered as distinct if they were separated by 2 or more branching points.

In contrast to the abundant synapses, the myelination of PV^+ axons at P14 was sparse and highly variable, ranging from no myelin to occasional axonal branches with several consecutive myelinated internodes (Fig. 2). While in adult animals the MBP immunolabel used to detect myelin precisely outlines myelinated stretches of axons, the internodes (Micheva et al., 2016), at P14 a discontinuous and weak MBP labeling was observed around some axons suggesting myelination in progress, and we refer to it here as incomplete myelin. Examples of complete (adult-like) and incomplete myelin are shown in Figure 2*A*′, *B*′. Of the five P14 pairs, one PV^+ interneuron had no myelin on its axon, 2 interneurons had only incomplete myelin on a few axonal stretches, and 2 interneurons had both complete and incomplete myelin (Fig. 3). Only 1 of the 5 P14 interneurons had an axon with considerable myelination on some of its branches.

The process of myelination does not appear to be occurring in the order of axonal branches; for example in pair MK190307, some third-, fourth-, and fifth-order axonal branches were myelinated, but no first- or second-order branches. In pair MK210204-3, one of the secondary axonal branches had substantial myelination, while the other one had only one internode with incomplete myelin. A clue as to why myelination proceeds in such a fashion may be provided by the uneven pattern of overall myelin distribution at this age. Thus, while myelin is already distributed rather uniformly in deeper cortical layers at P14 similarly to the adult animal, MBP immunolabel in layers 2/3, 4, and upper layer 5 at P14, revealed a mosaic distribution of patches with varying levels of myelination (Fig. 2*D*,*E*). Areas with no myelin sheaths were intercalated with similarly sized areas with incomplete myelin sheaths and areas with complete myelin sheaths, suggesting that the order of appearance of myelin on different axonal branches at this age may depend on where they are positioned relative to these areas. These areas likely represent the territories of individual oligodendrocytes, which, similarly to other glial cells, show tiling with nonoverlapping territories (Hughes et al., 2013; Buchanan et al., 2021). Oligodendrocytes are known to myelinate axons preferentially within 50 µm of their cell bodies (Murtie et al., 2007), which corresponds to the size of the areas with different myelination patterns that we observe (30-50 µm radius; Fig. 2*D*,*E*). Accordingly, within each tile with complete myelin, a myelinating oligodendrocyte could be discerned by its weak MBP immunolabel (Fig. 2*F*,*G*). Such weakly MBP-positive glial cells colabeled with the oligodendrocytic marker QKI (Fig. 2*H*). These observations suggest that the order of appearance of myelin on different axonal branches at this initial stage may depend on the timing of myelination by the specific oligodendrocyte within the territory of which they are positioned.

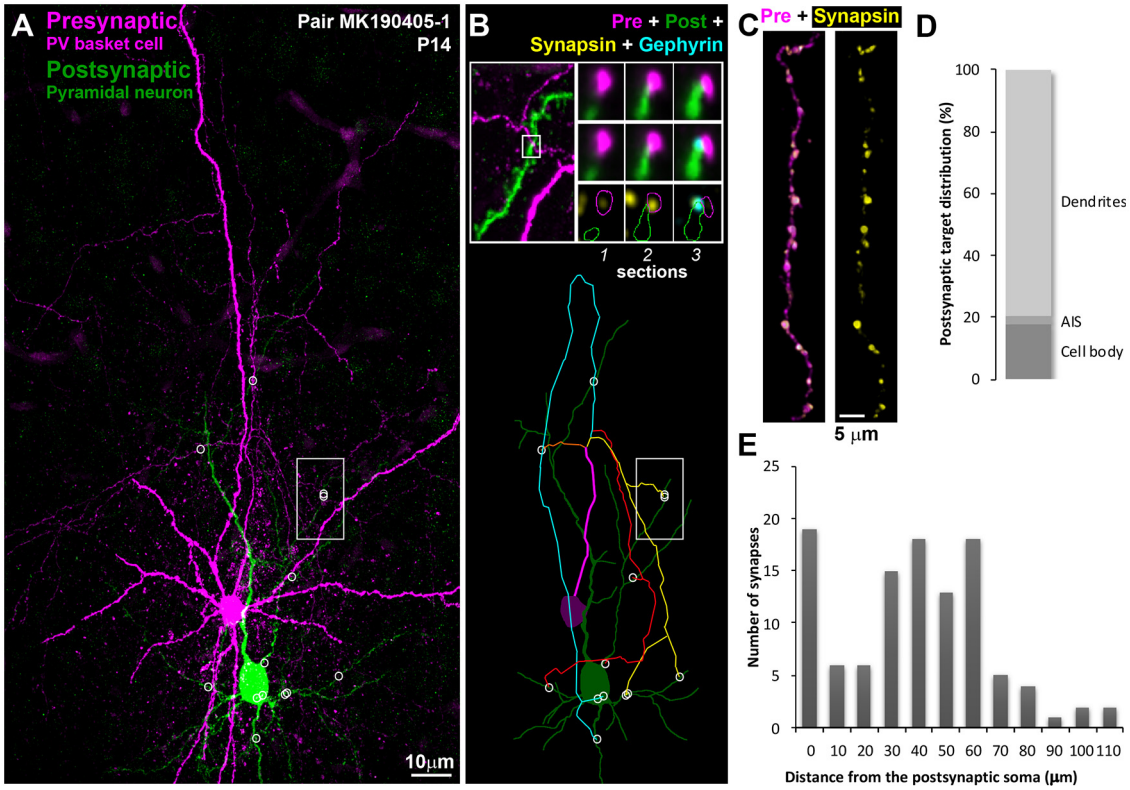

Figure 1. Synaptically connected PV$^+$ interneuron–pyramidal neuron pairs at P14. ***A***, MAX projection from pair MK190405-1, 480 serial ultrathin sections (100 nm each). Following ultrathin sectioning, the neurobiotin-filled presynaptic PV$^+$ interneuron was labeled with streptavidin Alexa-594 (magenta) and the Lucifer yellow-filled pyramidal neuron with anti-Lucifer yellow antibody (green). White circles represent locations of synapses. White rectangle represents the area shown at higher magnification in ***B*** (top). ***B***, Top left, Marked area from ***A*** showing the location of a synapse between the interneuronal axon and an apical dendritic branch of the pyramidal neuron. Top right, Three serial sections through the synapse identified to the left. The presynaptic bouton is immunoreactive for synapsin (yellow) on Sections 1 and 2, and gephyrin immunofluorescence (cyan) is observed at the postsynaptic side on Section 3. Bottom, Map of the connection. White circles represent synapses. There are four main axonal paths (represented by different colors) in this connection. ***C***, A stretch of the PV$^+$ interneuron axon immunolabeled with synapsin (yellow). ***D***, Distribution of postsynaptic targets at P14. ***E***, Frequency distribution of the distances of each synapse from the postsynaptic cell body in the P14 connections ($n = 109$).

Extensive myelination and synapse pruning in the third and fourth postnatal weeks

The above analysis reveals that, compared with older mice (1 month of age and older) (Micheva et al., 2021), most PV$^+$ interneurons at P14 have little or no myelin, but abundant synaptic connections. When do the axonal arbors of these interneurons change and how do myelination and synaptic pruning unfold in time? To better understand the sequence of these events, we analyzed 4 PV$^+$ interneuron pairs from P22 mice (Figs. 3 and 4; Extended Data Fig. 3-1) and then compared the P14 and P22 mice from this study with older mice from Micheva et al. (2021). Compared with P14 mice (22 ± 8 synapses), the number of synapses in a connection was not significantly different at P22 (16 ± 2), then dropped almost threefold to 6 ± 2 at 1 month (Fig. 4*A*). Subsequently, there appeared to be a trend toward an increase in the number of synapses to 10 ± 6 at 2 months and 10 ± 4 at 7 months, but the change was not statistically significant (Fig. 4*A*,*F*). To further validate these findings, we also analyzed the electrophysiological data from all neuronal pairs (only a fraction of these was used for AT analysis as stated in Materials and Methods). The amplitude of the presynaptic action potential-evoked IPSC correlates well with the number of synapses in a pair (Micheva et al., 2021); and in support of our AT results, we found that the IPSC amplitude of this larger sample of neuronal pairs showed a developmental pattern similar to the number of synapses (Fig. 4*B*,*G*).

The changes in myelination appeared to occur earlier than the decrease in synapse numbers. Thus, at P14, 3 of the 5 interneurons analyzed by AT had either no myelin or only small stretches of incomplete myelin on their axons, while all of the interneurons at P22 and later ages were myelinated. The average extent of myelin (complete myelin only) in the proximal 150 µm axonal arbor increased fivefold between P14 (55 ± 85 µm myelinated axon length per neuron) and P22 (273 ± 121 µm), and so did the myelination of the axonal paths in individual connections (6 ± 12% at P14, vs 25 ± 15% at P22) (Fig. 4*D*,*E*,*H*,*I*). During the same time, there was only a slight drop in the mean number of synapses per connection (from 22 ± 8 to 16 ± 2).

Following synapse pruning, adult connections consist of more proximally located synapses

Between P22 and 1 month, there is an almost threefold decrease in the number of synapses between a PV$^+$ interneuron and its postsynaptic target. Does this affect the topology of the connections in any way? Already at P14, the majority of synapses are distributed close to the postsynaptic cell body (average of average per neuron: 35 ± 10 µm from the soma), and this distribution does not change at P22 (35 ± 18 µm) and 1 month (44 ± 16 µm) (Fig. 5*A*). Subsequently, however, the PV$^+$ interneuron synapses are found closer to the postsynaptic soma (16 ± 16 µm at 2 months, and 25 ± 22 µm at 7 months; Fig. 5*A*,*J*). As a result, the proportion of synapses located on proximal dendrites within 20 µm of the postsynaptic cell body

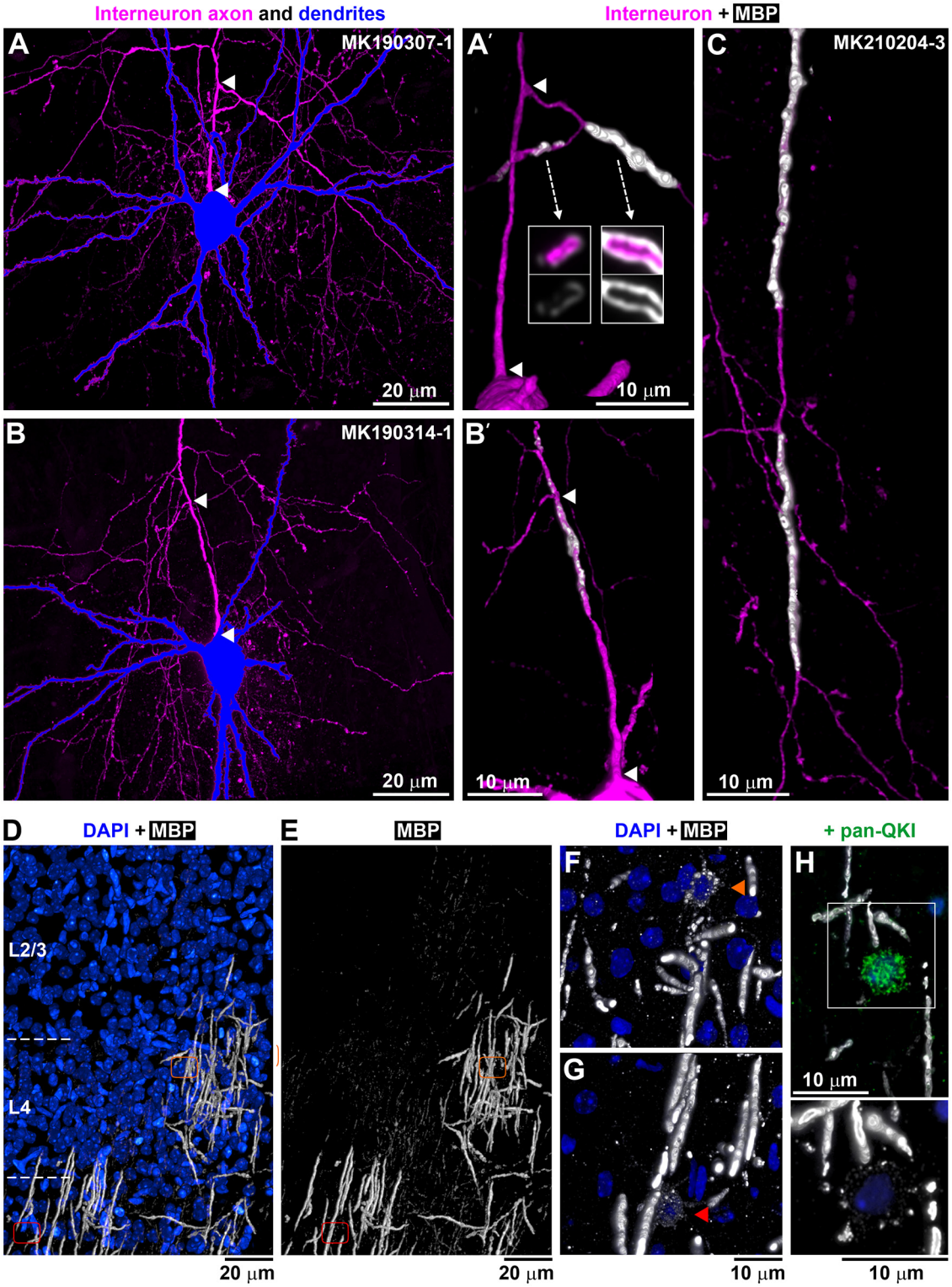

Figure 2. Axonal branching and myelination at P14. ***A***, ***B***, PV^+ interneurons from P14 neuronal pairs, with the soma and dendrites in blue and axon in magenta. MAX projections through all sections from pairs MK190307-1 (775 sections) and MK190314-1 (375 sections). ***A′***, ***B′***, Volume reconstruction of the axon initial segment of the interneurons in ***A*** (103 sections) and ***B***, respectively (136 sections). Arrowheads indicate the corresponding beginning and end of the first axonal segment from the soma to the first branching point. ***A′***, There are two tertiary axonal branches that are myelinated; the one going left is incompletely myelinated as seen by the uneven and weak MBP immunolabel. Arrows indicate single sections through the axonal branches. No myelination is observed before the first branching point. ***B′***, There is incomplete myelination before the first branching point as well as after that. No complete myelin was seen in this PV^+ interneuron. ***C***, Volume reconstruction of a tertiary axonal branch of the interneuron from pair MK210204-3 (192 sections), showing two completely myelinated internodes (39 and 36 μm long), separated by an unmyelinated axonal stretch (19 μm). ***D***, ***E***, MBP immunostaining of layers 2/3 and 4 at P14 (white; volume reconstruction from 529 sections). Blue represents DAPI-labeled nuclei. Areas with complete, incomplete, and no MBP immunolabel are seen. Orange and red outlines represent the locations of two different myelinating oligodendrocytes shown at higher magnification in ***F*** and ***G***. ***F***, ***G***, Myelinating oligodendrocytes characterized by weak MBP immunolabel within their cell bodies and proximal cell processes. Volume reconstruction from 36 sections (***F***) and 73 sections (***G***). ***H***, Weakly MBP-immunofluorescent oligodendrocytes (bottom, 13 sections volume reconstruction) colabeled with an antibody against panQKI, an oligodendrocytic marker (top, lower magnification).

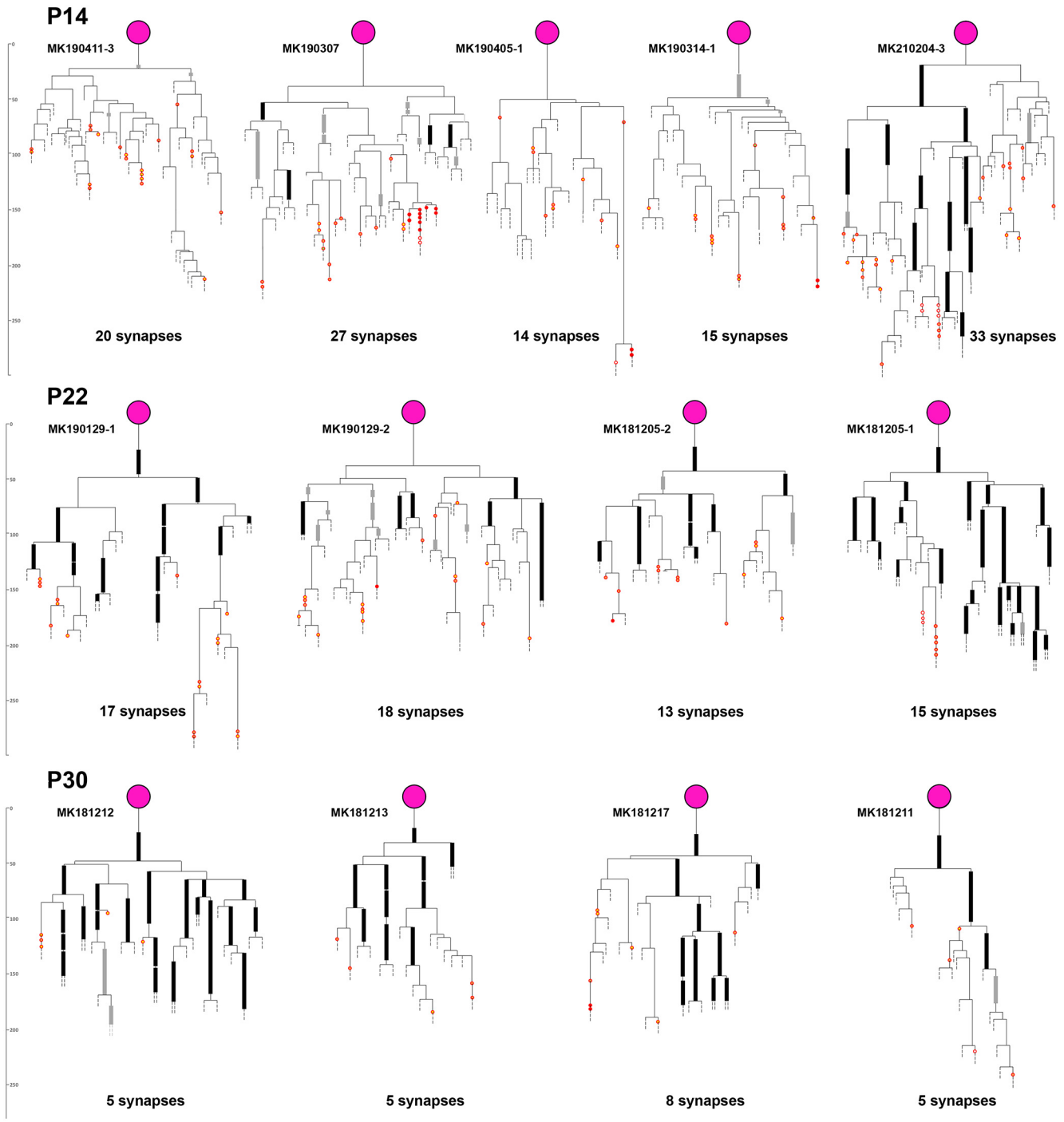

Figure 3. Axonograms of P14, P22, and P30 PV^+ interneurons. Thick black lines indicate myelinated internodes. Thick gray lines indicate incomplete myelination. Red circles represent synapses (full red represents on soma; orange with red represents on dendrite; yellow with red represents on spine; white with red represents on axon initial segment). Detailed axonograms and dendrograms of P14 and P22 pairs are shown in Extended Data Figure 3-1. The P30 pairs are from Micheva et al. (2021).

doubles after 1 month of age (Fig. 5*B*,*K*). One potential caveat of this analysis is that, among the older pairs, there were 3 cases where the postsynaptic neuron was not a pyramidal neuron, but another interneuron (and also 1 pair at P22), and we had previously observed that PV^+ interneuron to interneuron pairs tend to form synapses closer to the cell body compared with PV^+ interneuron to pyramidal neuron pairs (Micheva et al., 2021). We therefore repeated the analysis, now excluding these interneuron-on-interneuron pairs. This did not significantly change the average distance of the synapses from the postsynaptic soma (39 ± 9, 44 ± 16, and 24 ± 22 µm, excluding postsynaptic interneurons, vs 35 ± 13, 44 ± 16, and 20 ± 18 µm for all pairs, at <1 month, 1 month, and >1 month of age, respectively), neither the proportion of synapses located on the soma and proximal dendrites within 20 µm (27 ± 14%, 21 ± 29%, 59 ± 32 µm, excluding postsynaptic interneurons, vs 33 ± 22%, 21 ± 29%, 63 ± 26% for all pairs, at <1 month, 1 month, and >1 month of age, respectively) .

These results suggest that the changes in postsynaptic distribution of synapses lag behind the massive synapse pruning

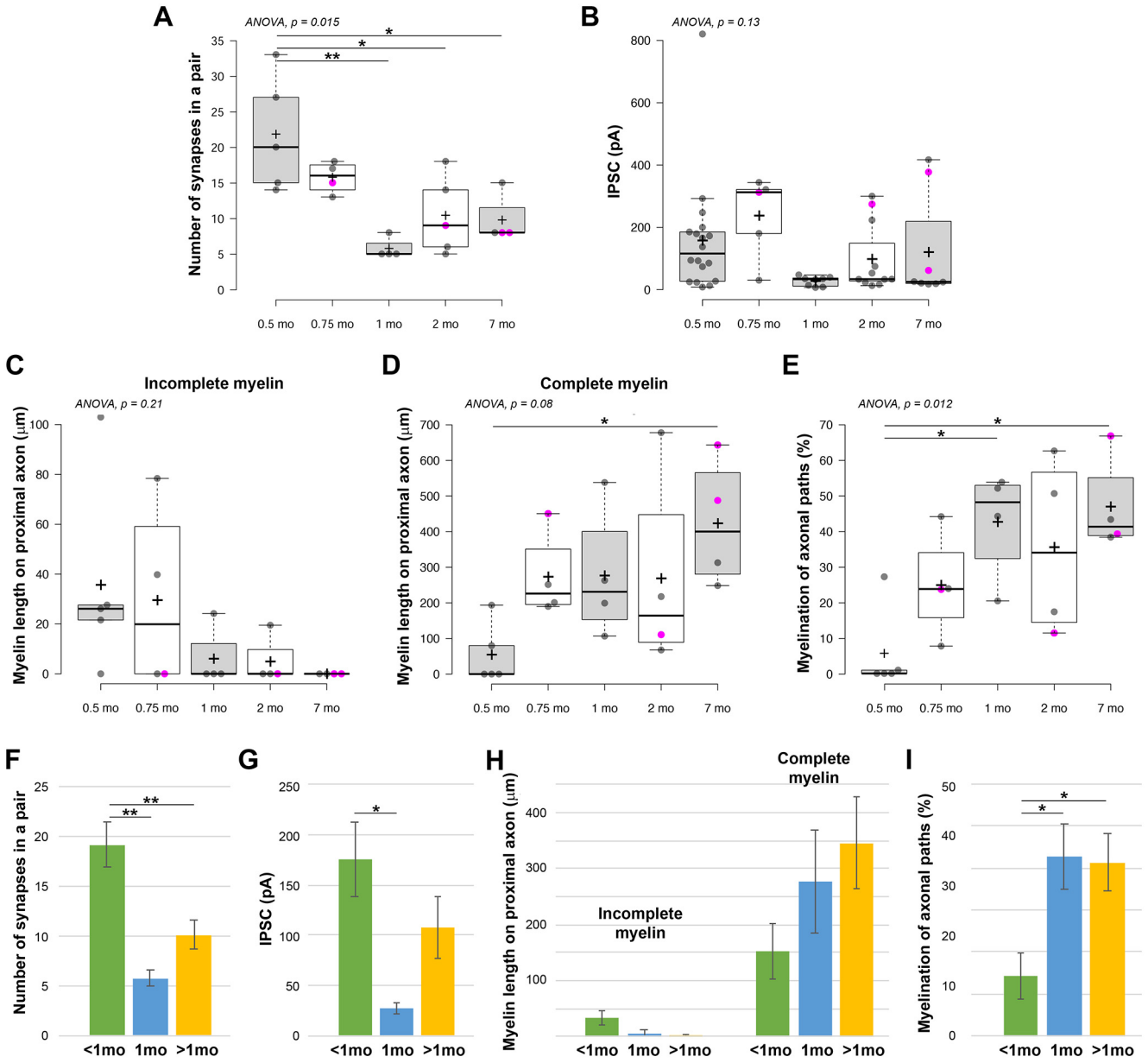

Figure 4. Changes in synapse numbers and in myelination of axonal paths of PV^+ interneuron connections during development. ***A***, Developmental changes in the number of synapses per PV^+ interneuron connection ($n = 5$ from 5 mice at P14, $n = 4$ from 2 mice at P22, $n = 4$ from 4 mice at 1 months, $n = 5$ from 5 mice at 2 months, and $n = 4$ from 4 mice at 7 months). ***B***, Changes in the amplitude of IPSC ($n = 18$ from 10 mice at P14, $n = 5$ from 3 mice at P22, $n = 8$ from 8 mice at 1 months, $n = 11$ from 10 mice at 2 months, and $n = 8$ from 6 mice at 7 months). ***C***, Changes in the total length of incomplete myelin on the proximal 150 µm of the axonal arbor. ***D***, Changes in the total length of complete myelin on the proximal 150 µm of the axonal arbor. ***E***, Changes in the myelination of axonal paths in the connections. ***A-E***, Magenta circles represent neuronal pairs with postsynaptic interneuron. $*p \leq 0.05$; $**p \leq 0.01$; one-way ANOVA with *post hoc* Tukey HSD test. Middle lines indicate the medians. Box limits indicate the 25th and 75th percentiles as determined by R software. Whiskers extend 1.5× the interquartile range from the 25th and 75th percentiles. Dots represent outliers. Crosses represent sample means. Data points are plotted as open circles. ***F-I***, Summary of developmental changes in synapse numbers in a connection (***F***), amplitude of IPSCs (***G***), myelin length (***H***), and myelination of axonal paths in a connection (***I***). $*p \leq 0.05$; $**p \leq 0.01$; one-way ANOVA with *post hoc* Tukey HSD test.

occurring at the end of the first postnatal month, and therefore cannot be explained by a potential selective removal of more distal synapses during pruning.

Synapse pruning likely occurs by removal of distal axonal branches

PV^+ interneurons send multiple axonal paths to form synapses with the postsynaptic neuron. These axonal paths diverge early on, most commonly starting at the first axonal branch point, and continue to split with increasing axonal branch orders. At P14, there were on average 8 ± 2 separate axonal paths (separated by 2 or more branch points), and at P22, 7 ± 2 axonal paths (Fig. 5*C*). Each of these axonal paths made on average 2.7 ± 0.7 synapses at P14, and 2.3 ± 0.2 at P22 (Fig. 5*D*); however, occasionally, as many as 8 or 9 synapses per axonal path were observed (e.g., pairs MK190307 and MK210204-3 at P14, and MK181205-1 at P22). This raises the question: does synaptic pruning of PV^+ interneurons involve removing of entire axonal branches, similarly to what happens with thalamocortical axons and axons of Cajal-Retzius interneurons in developing neocortex (Portera-Cailliau et al., 2005) and at the neuromuscular junction (Tapia et al., 2012), or are only individual synapses eliminated? The

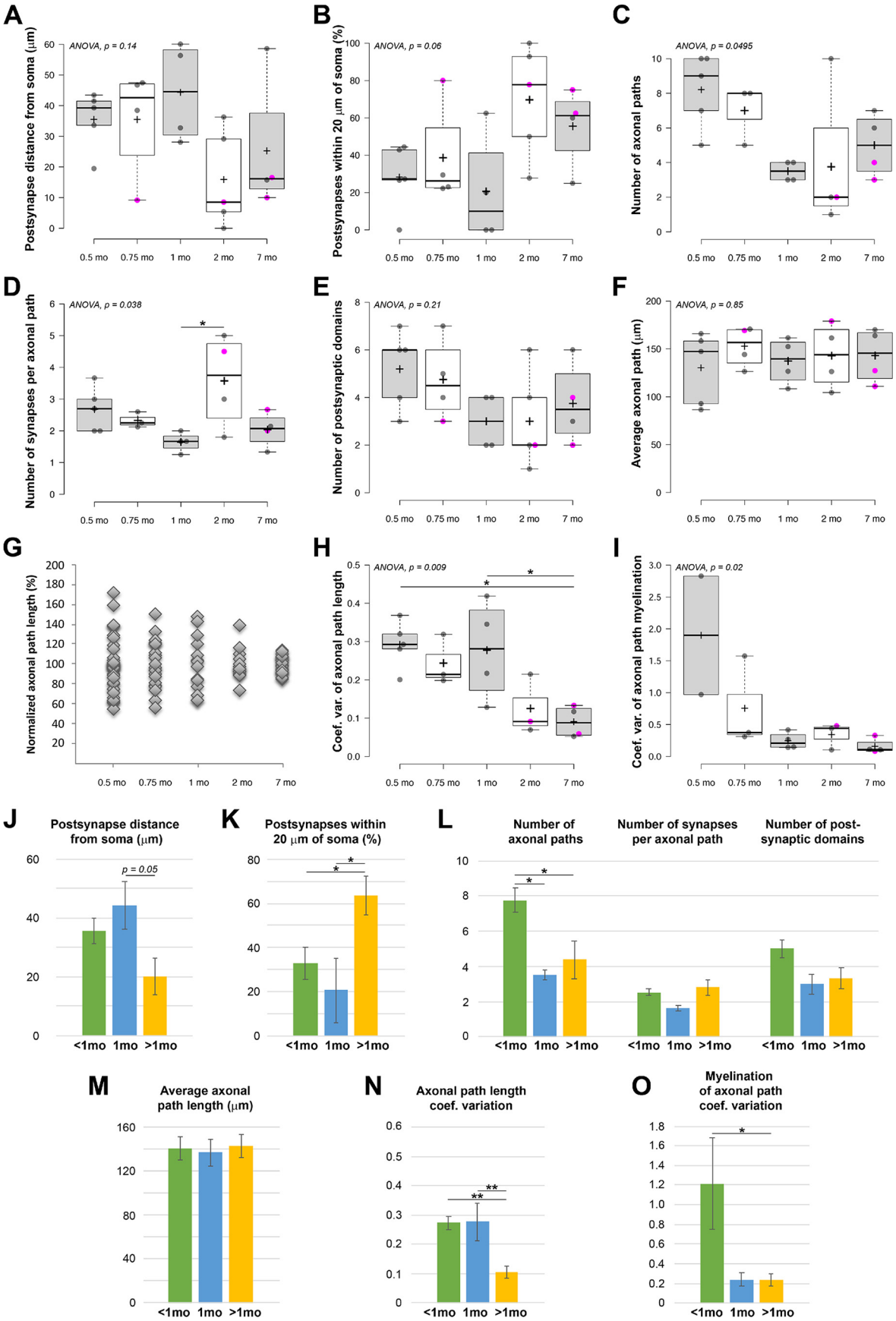

Figure 5. Developmental changes in the location of postsynaptic targets and axonal path lengths in the PV$^+$ interneuron connections. ***A-F***, Developmental changes in (***A***) postsynaptic target distance from soma, (***B***) the percentage of synapses within 20 μm of the postsynaptic soma, (***C***) the number of axonal paths in a connection, (***D***) the number of synapses per axonal path, (***E***) the number of targeted postsynaptic domains, and (***F***) the average axonal path per connection. Magenta circles represent neuronal pairs with postsynaptic interneuron. Center lines indicate

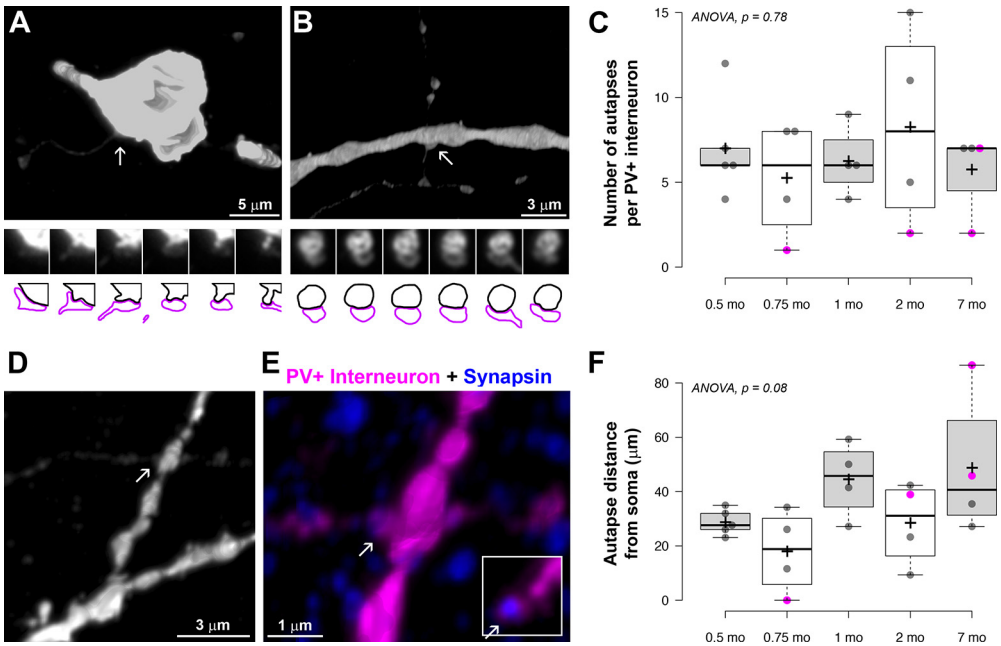

Figure 6. PV$^+$ interneuron autapses. ***A***, Example of an autapse on the interneuron soma (2-month-old pair MK190115-1). Volume reconstructions of the interneuron (streptavidin Alexa-594) on top and serial sections through the autapse on the bottom. The fluorescence intensity of the axon is much weaker compared with that of the soma or dendrites. In the color map of the autapses, magenta outline represents the presynaptic bouton and black represents the postsynaptic target. ***B***, Example of an autapse on a proximal dendrite (1-month-old pair MK181212). ***C***, Developmental changes in the number of autapses per PV$^+$ interneuron. Magenta circles represent neuronal pairs with postsynaptic interneuron. ***D***, Example of an autapse (white arrow) at P14 (pair MK190405-1). Volume reconstruction of the interneuron only (left, streptavidin Alexa-594) and zoomed in view of the synapse with the interneuron in magenta and synapsin immunolabel in blue (right). Right, Inset, Single section through the autapse showing the colocalization of synapsin (blue) and the presynaptic bouton fluorescence (magenta). ***E***, Developmental changes in the autapse target distribution. Magenta circles represent neuronal pairs with postsynaptic interneuron. ***C***, ***F***, There is no statistically significant difference depending on age as determined using one-way ANOVA. Middle lines indicate the medians. Box limits indicate the 25th and 75th percentiles as determined by R software. Whiskers extend 1.5× the interquartile range from the 25th and 75th percentiles. Dots represent outliers. Crosses represent sample means. Data points are plotted as open circles.

number of first- and second-order axonal branches in a connection remained stable during development (first branch: 1.9 ± 0.3 at <1 month, 1.8 ± 0.5 at 1 month, and 1.9 ± 0.6 at older than 1 month; second branch: 3.1 ± 0.6 at <1 month, 2.8 ± 0.5 at 1 month, and 2.4 ± 1.1 at older than 1 month). However, the number of separate axonal paths (separated by 2 or more branch points) decreased in half from 7.8 ± 2.0 at <1 month to 3.5 ± 0.6 at 1 month, and 4.4 ± 3.1 at older than 1 month (Fig. 5*C*,*L*). At the same time, the number of synapses per axonal path did not change (Fig. 5*D*,*L*), strongly suggesting that synaptic pruning predominantly removes entire distal axonal branches and not individual synapses. No significant changes in the number of postsynaptic domains (cell body, primary dendrite with it branches, or axon initial segment) receiving synaptic input was detected (Fig. 5*E*,*L*).

←

the medians. Box limits indicate the 25th and 75th percentiles as determined by R software. Whiskers extend 1.5× the interquartile range from the 25th and 75th percentiles. Dots represent outliers. Crosses represent sample means. Data points are plotted as open circles. ***G***, Axonal path lengths normalized to the average per connection. While the variations in the average axonal path length between pairs does not change much, as seen in ***F***, the length of individual axonal paths within a connection becomes much more uniform with age. ***H***, Changes in the coefficient of variation of axonal path lengths. ***I***, Changes in the coefficient of variation of the percent myelination of axonal paths. ***J-N***, Summary of developmental changes in (***J***) postsynaptic target distance from soma, (***K***) the percentage of synapses within 20 µm of the postsynaptic soma, (***L***) number of axonal paths, synapses per axonal path, and targeted postsynaptic domains, (***M***) average axonal path length, (***N***) coefficients of variation of axonal path length, and (***O***) coefficients of variation of percent myelination of axonal paths. *$p \leq 0.05$; **$p \leq 0.01$; one-way ANOVA with *post hoc* Tukey HSD test.

Prolonged period of connection refinement results in more uniform axonal path lengths and myelination in the mature animal

Does the axon arbor continue to change after the initial period of synapse pruning (P22 to 1 month)? The average axonal path length (the average of the connection averages) remained constant throughout development, between 130 and 150 µm (Fig. 5*F*). However, there was a remarkable change in the variability of the length of the axonal paths in a connection. At the youngest age, P14, the lengths of the different paths in a connection varied by as much as 60% and more from the average, and similar high variability persisted at P22 and at 1 month with path lengths varying as much as 50% from the average. After 1 month, the lengths of the different paths comprising the connection become much more uniform, and at 7 months axonal path lengths deviated by <15% from the average length for the connection (Fig. 5*G*). This is reflected in the significant decrease in the coefficient of variation of axonal path lengths at 7 months (Fig. 5*H*,*N*). The extent of myelination of the different axonal paths in a connection also became more consistent, and there was a significant reduction in the coefficient of variation of the percent myelination of axonal paths after 1 month (Fig. 5*I*,*O*).

Autapse numbers remain stable between P14 and 7 months

PV$^+$ interneurons also form autapses (i.e., synapses onto themselves) shown to have important functional roles, such as regulating spike-timing precision (Bacci and Huguenard, 2006) and tuning to γ oscillations (Deleuze et al., 2019). Examples of autapses are shown in Figure 6*A*, *B*, *D*, *E*. Although both the axon and its postsynaptic target in this case are filled with the same dye,

the fluorescence in the axon is weaker and thus can be detected as a separate entity when analyzing the images. Autapses are also known to have large presynaptic varicosities (Tamás et al., 1997b), further aiding in their identification. At P14 and P22 autapses were observed in all the neuronal pairs ($n = 9$) and their number ranged from 1 to 12 per interneuron, with an average of 6 ± 3. Contrary to what is observed with intercell synapses, the average number of autapses per interneuron remained constant with age (Fig. 6*C*). Autapses were distributed proximally to the soma, and no change in target distribution was detected at the different ages (Fig. 6*F*). No correlation was seen between the number of autapses and the number of intercell synapses per connection ($R = 0.23$) between either the distribution of autapses and intercell synapses relative to the soma ($R = 0.003$).

It was reported recently that PV^+ interneurons with smaller autaptic responses make stronger connections with other PV^+ interneurons (Deleuze et al., 2019). Consistent with this, we observed that 3 of the 4 PV^+ interneurons in our sample that synapsed onto other interneurons, had only 1 or 2 autapses (the fourth one had 7), while none of the 17 PV^+ interneurons synapsing onto a pyramidal neuron had fewer than 4 autapses.

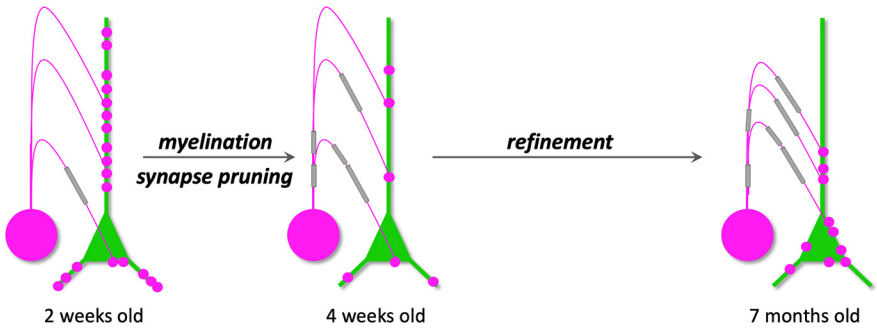

Figure 7. Summary of the main developmental changes in PV^+ interneuron individual connections. Substantial reorganization of the PV^+ interneuron connections occurs in the second half of the first postnatal month as axons become myelinated and the number of synapses decreases by threefold. Connection refinement continues beyond this, with the postsynaptic targets of PV interneurons gradually shifting to more proximal locations, and the length of axonal paths and their myelin becoming conspicuously uniform per connection by postnatal month 7. Magenta represents PV^+ interneuron. Green represents postsynaptic neuron. Gray represents myelin.

Discussion

PV^+ basket cells in mammalian neocortex have distinct axonal arbors, characterized by extensive branching, intermittent myelination, and abundant synapses surrounding cell bodies of neighboring pyramidal neurons and within the neuropil. Our results reveal the extensive reorganization of the axon-myelin unit following the formation of the initial immature connectivity of PV^+ interneurons (Fig. 7). At the end of the second postnatal week, PV^+ basket cells have highly branched axons that are rarely myelinated and form abundant synaptic contacts with pyramidal neurons. During the third and fourth postnatal week, the proximal axons of PV^+ interneurons become rapidly myelinated, and massive synapse pruning occurs. This pruning does not affect the autapses that PV^+ interneurons form on themselves. More subtle reorganizations continue throughout the examined period, until postnatal month 7. They include a shift of the postsynaptic targets of PV^+ interneurons to more proximal locations and a significant decrease of the variability of the length of axonal paths in each connection.

Developmental changes in myelination of PV^+ interneurons

Myelination of the axon is a characteristic feature of PV^+ basket cells in neocortex (De Felipe et al., 1986; Somogyi and Soltész, 1986; Micheva et al., 2016; Stedehouder et al., 2017), despite the fact that the great majority of their connections are local (Packer and Yuste et al., 2011). Deficits in myelination can affect multiple aspects of PV^+ interneuron development, such as their axonal arborization, synaptic connectivity, and firing rate (Benamer et al., 2020). PV^+ interneuron myelin likely has multiple roles, including energy conservation (Hartline and Colman, 2007) and nutrient support (Fünfschilling et al., 2012; Lee et al., 2012), of these fast-spiking neurons known for their high-energy demands (Kann et al., 2014), as well as increase in conduction velocity along the axon (Micheva et al., 2021). Our present results show that, during development, myelination of the proximal PV^+ interneuron axon occurs rapidly during the second half of the first postnatal month, mostly in the third postnatal week. This is also the time when the spiking frequency of PV^+ interneurons greatly increases (Okaty et al., 2009; Miyamae et al., 2017), resulting presumably in increased energy demands, and basket cells differentiate into "fast signaling devices" (Doischer et al., 2008) needing faster conduction of axon potentials along the axon. By the end of the first postnatal month, the extent of myelination of the proximal axonal arbor (up to 150 μm from soma), as well as the myelination of the axonal paths connecting the interneurons with nearby cells, reaches adult levels. Because the overall cortical myelination is known to increase throughout much of adulthood (Hill et al., 2018; Hughes et al., 2018), these results suggest that PV^+ interneurons may be acquiring their myelin earlier compared with other neurons. Further studies are needed to directly compare the developmental course of myelination of PV^+ interneurons to other sources of neocortical myelinated axons, such as pyramidal neurons or thalamocortical projections. Interestingly, the extent of myelination of individual PV^+ interneurons varies greatly at all ages, and we recently showed that it correlates with the conduction velocity along the axon (Micheva et al., 2021). It remains to be seen whether it also correlates with the activity level of interneurons, and, correspondingly, their energy demands.

PV^+ interneuron synapse pruning

In the second half of the first postnatal month, the number of synapses per connection declines to one-third of the P14 numbers. The observed large drop in the number of synapses per connection was rather surprising because, although pruning of PV^+ interneuron synapses is known to occur at this developmental stage, it is counterbalanced by new synapse formation (Chattopadhyaya et al., 2004). Thus, during the second half of the first postnatal month, there is no significant change in the number of PV^+ perisomatic synapses in layer 2/3 of rat medial entorhinal cortex (Berggaard et al., 2018) and an increase in perisomatic PV^+ synapses in mouse visual cortex organotypic cultures (Chattopadhyaya et al., 2004), as well as an increase in the total number of all inhibitory synapses (Micheva and Beaulieu, 1996; De Felipe et al., 1997). Our findings suggest that the overall increase in PV^+ synapse numbers in cortex during the first postnatal month is most likely because of PV^+ basket cells continuing to extend their axons and contacting more and more postsynaptic neurons, thus masking the drop in the number of synapses per individual connection. The decrease in PV^+

synapses per connection appears to be because of retraction of distal axonal branches, and not removal of individual synapses. Indeed, as shown in organotypic slices from mouse visual cortex (Wu et al., 2012), the axons of PV^+ basket cells at this age are very dynamic. New axonal branches continuously emerge and form synapses, while existing axonal branches retract, and branch addition is slightly more prevalent than branch elimination. Inhibitory synapse elimination is regulated by activity-dependent mechanisms, including GABA neurotransmission (Wu et al., 2012), via specialized GABA-receptive microglia (Favuzzi et al., 2021) and potentially other mechanisms (e.g., Buchanan et al., 2021). Interestingly, the number of autapses made by PV^+ interneurons does not undergo pruning, suggesting that they follow different developmental rules compared with synapses. While autapse formation and maintenance may be an intrinsic property of PV^+ basket cells, synapse formation involves a two-way communication with the postsynaptic neuron. Previous studies have shown that inhibitory synapses undergo pruning, but to a lesser extent than excitatory synapses (De Felipe et al., 1997). Our results strongly suggest that PV^+ basket cells initially form exuberant synaptic connections that are subsequently refined as weaker or inappropriate synapses are removed. The magnitude of this refinement (a threefold reduction in synapse numbers per connection), however, can be appreciated only when focusing on individual neuron-to-neuron connections, as done in the current study, because synapse pruning is masked to a large extent by the formation of new synapses.

Limitations

There are several caveats to our study to take into account when interpreting the results. Because we used W. floribunda lectin labeling of perineuronal nets to identify PV^+ interneurons, and perineuronal net development is activity-regulated (Dityatev et al., 2007), it is possible that this method of identification selected specifically for PV^+ interneurons with higher activity levels and/or more advanced maturation at P14 and P22. Consequently, the developmental changes that we report may be underestimating the magnitude of axonal and synaptic reorganization of neocortical PV^+ basket cells during the first postnatal month. Additionally, the PV^+ interneurons that were analyzed come from different cortical layers (layers 3-6) of entorhinal and perirhinal cortex. It is highly likely that this introduces additional variations in their axonal organization and connectivity that may be obscuring some developmental trends. Other important limitations come from our choice of experimental methods. Immunofluorescent AT, while providing the resolution to reliably trace PV^+ interneuron axons and their myelin sheath, and identify the great majority of synapses, requires chemical fixation and ultrathin sectioning of the tissue, which is incompatible with live imaging. Developmental trajectories are inferred from static images at different time points, which introduces ambiguities. For example, we report that the decrease in synapse numbers at 1 month of age is accompanied by a decrease in the number of axonal paths, but not the number of synapses per axonal path. While this strongly suggests that synapse pruning is largely accomplished by removal of entire distal axonal branches, similarly to what is observed in other systems (Portera-Cailliau et al., 2005; Tapia et al., 2012), it does not rule out the possibility that individual synapses along remaining axonal paths are removed as well.

Functional implications of the developmental changes of PV^+ interneuron connectivity and myelination

The profound changes in axon myelination and synaptic connections of PV^+ interneurons during the second half of the first postnatal month coincide with rapid behavioral changes. The PV^+ interneurons analyzed in this study were located in entorhinal and perirhinal cortices, higher-order cortical regions involved in spatial navigation (Moser et al., 2008) and object recognition memory (Squire et al., 2007). Mouse pups open their eyes at P14 and begin venturing outside of their nest around P16 (König, 2012), and this exploratory activity greatly increases by the end of the third postnatal week, a period that overlaps with the myelination and immediately precedes the massive synapse pruning of individual PV^+ connections that we report. Rodent exploration behaviors, however, continue to mature until the third postnatal month (Wills et al., 2014); and consistent with this, we observe more gradual alterations of the PV^+ interneuron axonal arbors and synaptic circuitry past 1 and 2 months of age. These late circuit refinements include a shift of the postsynaptic target locations closer to the postsynaptic cell body, thus ensuring stronger inhibitory control of the postsynaptic neuron. It is notable, however, that PV^+ basket cell axons have a strong preference for perisomatic postsynaptic targets already at P14 as seen from our results. This preference likely appears much earlier, between P7 and P9, when a subset of inhibitory axons, which presumably includes PV^+ basket cell axons, begin exhibiting a preference for soma innervation, as shown by electron microscopic mapping of inhibitory circuits in the developing mouse somatosensory cortex (Gour et al., 2021). During early development, the establishment of this target preference is likely achieved by pruning of more distal synapses, as evidenced by the decrease in the density of such synapses along the soma-preferring axons (Gour et al., 2021). The continued shift to perisomatic synapse locations later in development that we describe here may be very similar and achieved through ongoing synapse turnover, albeit at lower levels as observed for GABA synapses in general (Marik et al., 2010; Chen et al., 2011), with new synapses formed closer to the postsynaptic cell bodies, and existing more distal synapses eliminated.

Another change in PV^+ interneuron connectivity reported here is the rather striking uniformity of the length of the axonal paths within individual PV^+ interneuron connection that is achieved later in development, after the first postnatal month. PV^+ interneurons typically connect to their postsynaptic target via several different axonal paths (Micheva et al., 2021), which may provide redundancy to ensure reliable neurotransmission by guarding against possible branch failures. Alternatively, this structural arrangement may enable a much more nuanced communication by allowing differential activation of the paths at axonal branch points (Debanne, 2004). In either case, because the extent of myelination of the different axonal paths within a connection also tends to become more even with age, these observations reveal that continued microcircuit refinement results in a remarkably precise organization of PV^+ interneuron axonal arbors, providing the structural support for their robust inhibitory effect and fine temporal precision. Together, these refinements toward uniform path length and myelination suggest both redundancy in the connection leading to an increase in the "safety factor" of PV^+ interneuron to target transmission and uniform latency of the synaptic transmission at all of a particular afferent cell's branches.

In conclusion, here we have characterized the development of PV^+ interneuron connectivity by focusing on the minimal element of the neuronal circuitry, one neuron synapsing onto one other neuron. Essential for this analysis is the comprehensive investigation of the axon-myelin unit (Simons et al., 2014; Suminaite et al., 2019) and the inclusion of the postsynapse as part of this unit. Our study reveals the elaborate organization and fine precision of the mature PV^+ interneuron connectivity

and how it evolves during development. Future studies are needed to unravel the complex interactions between the presynaptic and postsynaptic neuron, and the myelinating oligodendrocytes, that underlie these changes.

References

Ahmari SE, Buchanan J, Smith SJ (2000) Assembly of presynaptic active zones from cytoplasmic transport packets. Nat Neurosci 3:445–451.

Aliaga Maraver JJ, Mata S, Benavides-Piccione R, De Felipe J, Pastor L (2018) A method for the symbolic representation of neurons. Front Neuroanat 12:106.

Bacci A, Huguenard JR (2006) Enhancement of spike-timing precision by autaptic transmission in neocortical inhibitory interneurons. Neuron 49:119–130.

Benamer N, Vidal M, Balia M, Angulo MC (2020) Myelination of parvalbumin interneurons shapes the function of cortical sensory inhibitory circuits. Nat Commun 11:5151.

Berggaard N, Bjerke IE, Paulsen AE, Hoang L, Skogaker NE, Witter MP, van der Want JJ (2018) Development of parvalbumin-expressing basket terminals in layer ii of the rat medial entorhinal cortex. eNeuro 5: ENEURO.0438-17.2018.

Buchanan J, Elabbady L, Collman F, Jorstad NL, Bakken TE, Ott C, Glatzer J, Bleckert AA, Bodor AL, Brittan D, Bumbarger DJ, Mahalingam G, Seshamani S, Schneider-Mizell C, Takeno MM, Torres R, Yin W, Hodge RD, Castro M, Dorkenwald S, et al. (2021) Oligodendrocyte precursor cells prune axons in the mouse neocortex. bioRxiv 446047.

Busse B, Smith SJ (2013) Automated analysis of a diverse synapse population. PLoS Comput Biol 9:e1002976.

Buzsáki G, Wang XJ (2012) Mechanisms of gamma oscillations. Annu Rev Neurosci 35:203–225.

Cardin JA (2018) Inhibitory interneurons regulate temporal precision and correlations in cortical circuits. Trends Neurosci 41:689–700.

Cardin JA, Carlén M, Meletis K, Knoblich U, Zhang F, Deisseroth K, Tsai LH, Moore CI (2009) Driving fast-spiking cells induces gamma rhythm and controls sensory responses. Nature 459:663–667.

Chariker L, Shapley R, Young LS (2018) Rhythm and synchrony in a cortical network model. J Neurosci 38:8621–8634.

Chattopadhyaya B, Di Cristo G, Higashiyama H, Knott GW, Kuhlman SJ, Welker E, Huang ZJ (2004) Experience and activity-dependent maturation of perisomatic GABAergic innervation in primary visual cortex during a postnatal critical period. J Neurosci 24:9598–9611.

Chen JL, Lin WC, Cha JW, So PT, Kubota Y, Nedivi E (2011) Structural basis for the role of inhibition in facilitating adult brain plasticity. Nat Neurosci 14:587–594.

Collman F, Buchanan J, Phend KD, Micheva KD, Weinberg RJ, Smith SJ (2015) Mapping synapses by conjugate light-electron array tomography. J Neurosci 35:5792–5807.

Debanne D (2004) Information processing in the axon. Nat Rev Neurosci 5:304–316.

De Felipe J, Marco P, Fairén A, Jones EG (1997) Inhibitory synaptogenesis in mouse somatosensory cortex. Cereb Cortex 7:619–634.

De Felipe J, Hendry SH, Jones EG (1986) A correlative electron microscopic study of basket cells and large GABAergic neurons in the monkey sensory-motor cortex. Neuroscience 17:991–1009.

del Río JA, de Lecea L, Ferrer I, Soriano E (1994) The development of parvalbumin-immunoreactivity in the neocortex of the mouse. Brain Res Dev Brain Res 81:247–259.

Deleuze C, Bhumbra GS, Pazienti A, Lourenço J, Mailhes C, Aguirre A, Beato M, Bacci A (2019) Strong preference for autaptic self-connectivity of neocortical PV interneurons facilitates their tuning to γ-oscillations. PLoS Biol 17:e3000419.

Dityatev A, Brückner G, Dityateva G, Grosche J, Kleene R, Schachner M (2007) Activity-dependent formation and functions of chondroitin sulfate-rich extracellular matrix of perineuronal nets. Dev Neurobiol 67:570–588.

Doischer D, Hosp JA, Yanagawa Y, Obata K, Jonas P, Vida I, Bartos M (2008) Postnatal differentiation of basket cells from slow to fast signaling devices. J Neurosci 28:12956–12968.

Favuzzi E, Huang S, Saldi GA, Binan L, Ibrahim LA, Fernández-Otero M, Cao Y, Zeine A, Sefah A, Zheng K, Xu Q, Khlestova E, Farhi SL, Bonneau R, Datta SR, Stevens B, Fishell G (2021) GABA-receptive microglia selectively sculpt developing inhibitory circuits. Cell 184:4048–4063.e32.

Ferguson BR, Gao WJ (2018) PV interneurons: critical regulators of E/I balance for prefrontal cortex-dependent behavior and psychiatric disorders. Front Neural Circuits 12:37.

Fünfschilling U, Supplie LM, Mahad D, Boretius S, Saab AS, Edgar J, Brinkmann BG, Kassmann CM, Tzvetanova ID, Möbius W, Diaz F, Meijer D, Suter U, Hamprecht B, Sereda MW, Moraes CT, Frahm J, Goebbels S, Nave KA (2012) Glycolytic oligodendrocytes maintain myelin and long-term axonal integrity. Nature 485:517–521.

Gour A, Boergens KM, Heike N, Hua Y, Laserstein P, Song K, Helmstaedter M (2021) Postnatal connectomic development of inhibition in mouse barrel cortex. Science 371:eabb4534.

Hartline DK, Colman DR (2007) Rapid conduction and the evolution of giant axons and myelinated fibers. Curr Biol 17:R29–R35.

Hill RA, Li AM, Grutzendler J (2018) Lifelong cortical myelin plasticity and age-related degeneration in the live mammalian brain. Nat Neurosci 21:683–695.

Hoppenrath K, Härtig W, Funke K (2016) Intermittent theta-burst transcranial magnetic stimulation alters electrical properties of fast-spiking neocortical interneurons in an age-dependent fashion. Front Neural Circuits 10:22.

Hughes EG, Kang SH, Fukaya M, Bergles DE (2013) Oligodendrocyte progenitors balance growth with self-repulsion to achieve homeostasis in the adult brain. Nat Neurosci 16:668–676.

Hughes EG, Orthmann-Murphy JL, Langseth AJ, Bergles DE (2018) Myelin remodeling through experience-dependent oligodendrogenesis in the adult somatosensory cortex. Nat Neurosci 21:696–706.

Kann O, Papageorgiou IE, Draguhn A (2014) Highly energized inhibitory interneurons are a central element for information processing in cortical networks. J Cereb Blood Flow Metab 34:1270–1282.

Kawaguchi Y, Kubota Y (1998) Neurochemical features and synaptic connections of large physiologically identified GABAergic cells in the rat frontal cortex. Neuroscience 85:677–701.

König B (2012) The behavior of the house mouse. In: The laboratory mouse, Ed 2, pp 367–381. Amsterdam: Elsevier.

Lee Y, Morrison BM, Li Y, Lengacher S, Farah MH, Hoffman PN, Liu Y, Tsingalia A, Jin L, Zhang PW, Pellerin L, Magistretti PJ, Rothstein JD (2012) Oligodendroglia metabolically support axons and contribute to neurodegeneration. Nature 487:443–448.

Lim L, Mi D, Llorca A, Marín O (2018) Development and functional diversification of cortical interneurons. Neuron 100:294–313.

Marik SA, Yamahachi H, McManus JN, Szabo G, Gilbert CD (2010) Axonal dynamics of excitatory and inhibitory neurons in somatosensory cortex. PLoS Biol 8:e1000395.

Micheva KD, Beaulieu C (1996) Quantitative aspects of synaptogenesis in the rat barrel field cortex with special reference to GABA circuitry. J Comp Neurol 373:340–354.

Micheva KD, Busse B, Weiler NC, O'Rourke N, Smith SJ (2010) Single-synapse analysis of a diverse synapse population: proteomic imaging methods and markers. Neuron 68:639–653.

Micheva KD, Wolman D, Mensh BD, Pax E, Buchanan J, Smith SJ, Bock DD (2016) A large fraction of neocortical myelin ensheathes axons of local inhibitory neurons. Elife 5:e15784.

Micheva KD, Kiraly M, Perez MM, Madison DV (2021) Conduction velocity along the local axons of parvalbumin interneurons correlates with the degree of axonal myelination. Cereb Cortex 31:3374–3392.

Miyamae T, Chen K, Lewis DA, Gonzalez-Burgos G (2017) Distinct physiological maturation of parvalbumin-positive neuron subtypes in mouse prefrontal cortex. J Neurosci 37:4883–4902.

Montgomery JM, Pavlidis P, Madison DV (2001) Pair recordings reveal all-silent synaptic connections and the postsynaptic expression of long-term potentiation. Neuron 29:691–701.

Moser EI, Kropff E, Moser MB (2008) Place cells, grid cells, and the brain's spatial representation system. Annu Rev Neurosci 31:69–89.

Murtie JC, Macklin WB, Corfas G (2007) Morphometric analysis of oligodendrocytes in the adult mouse frontal cortex. J Neurosci Res 85:2080–2086.

Okaty BW, Miller MN, Sugino K, Hempel CM, Nelson SB (2009) Transcriptional and electrophysiological maturation of neocortical fast-spiking GABAergic interneurons. J Neurosci 29:7040–7052.

Packer AM, Yuste R (2011) Dense, unspecific connectivity of neocortical parvalbumin-positive interneurons: a canonical microcircuit for inhibition? J Neurosci 31:13260–13271.

Pavlidis P, Madison DV (1999) Synaptic transmission in pair recordings from CA3 pyramidal cells in organotypic culture. J Neurophysiol 81:2787–2797.

Portera-Cailliau C, Weimer RM, De Paola V, Caroni P, Svoboda K (2005) Diverse modes of axon elaboration in the developing neocortex. PLoS Biol 3:e272.

Pouille F, Scanziani M (2001) Enforcement of temporal fidelity in pyramidal cells by somatic feed-forward inhibition. Science 293:1159–1163.

Rudy B, Fishell G, Lee S, Hjerling-Leffler J (2011) Three groups of interneurons account for nearly 100% of neocortical GABAergic neurons. Dev Neurobiol 71:45–61.

Schindelin J, Arganda-Carreras I, Frise E, Kaynig V, Longair M, Pietzsch T, Preibisch S, Rueden C, Saalfeld S, Schmid B, Tinevez JY, White DJ, Hartenstein V, Eliceiri K, Tomancak P, Cardona A (2012) Fiji: an open-source platform for biological-image analysis. Nat Methods 9:676–682.

Simons M, Misgeld T, Kerschensteiner M (2014) A unified cell biological perspective on axon-myelin injury. J Cell Biol 206:335–345.

Somogyi P, Kisvárday ZF, Martin KA, Whitteridge D (1983) Synaptic connections of morphologically identified and physiologically characterized large basket cells in the striate cortex of cat. Neuroscience 10:261–294.

Somogyi P, Soltész I (1986) Immunogold demonstration of GABA in synaptic terminals of intracellularly recorded, horseradish peroxidase-filled basket cells and clutch cells in the cat's visual cortex. Neuroscience 19:1051–1065.

Southwell DG, Paredes MF, Galvao RP, Jones DL, Froemke RC, Sebe JY, Alfaro-Cervello C, Tang Y, Garcia-Verdugo JM, Rubenstein JL, Baraban SC, Alvarez-Buylla A (2012) Intrinsically determined cell death of developing cortical interneurons. Nature 491:109–113.

Spitzer M, Wildenhain J, Rappsilber J, Tyers M (2014) BoxPlotR: a web tool for generation of box plots. Nat Methods 11:121–122.

Squire LR, Wixted JT, Clark RE (2007) Recognition memory and the medial temporal lobe: a new perspective. Nat Rev Neurosci 8:872–883.

Stedehouder J, Couey JJ, Brizee D, Hosseini B, Slotman JA, Dirven CM, Shpak G, Houtsmuller AB, Kushner SA (2017) Fast-spiking parvalbumin interneurons are frequently myelinated in the cerebral cortex of mice and humans. Cereb Cortex 27:5001–5013.

Suminaite D, Lyons DA, Livesey MR (2019) Myelinated axon physiology and regulation of neural circuit function. Glia 67:2050–2062.

Tamás G, Buhl EH, Somogyi P (1997a) Fast IPSPs elicited via multiple synaptic release sites by different types of GABAergic neurone in the cat visual cortex. J Physiol 500:715–738.

Tamás G, Buhl EH, Somogyi P (1997b) Massive autaptic self-innervation of GABAergic neurons in cat visual cortex. J Neurosci 17:6352–6364.

Tapia JC, Wylie JD, Kasthuri N, Hayworth KJ, Schalek R, Berger DR, Guatimosim C, Seung HS, Lichtman JW (2012) Pervasive synaptic branch removal in the mammalian neuromuscular system at birth. Neuron 74:816–829.

Ting JT, Lee BR, Chong P, Soler-Llavina G, Cobbs C, Koch C, Zeng H, Lein E (2018) Preparation of acute brain slices using an optimized N-methyl-D-glucamine protective recovery method. J Vis Exp 132:53825.

Wehr M, Zador AM (2003) Balanced inhibition underlies tuning and sharpens spike timing in auditory cortex. Nature 426:442–446.

Wills TJ, Muessig L, Cacucci F (2014) The development of spatial behaviour and the hippocampal neural representation of space. Philos Trans R Soc Lond B Biol Sci 369:20130409.

Wong FK, Bercsenyi K, Sreenivasan V, Portalés A, Fernández-Otero M, Marín O (2018) Pyramidal cell regulation of interneuron survival sculpts cortical networks. Nature 557:668–673.

Wu X, Fu Y, Knott G, Lu J, Di Cristo G, Huang ZJ (2012) GABA signaling promotes synapse elimination and axon pruning in developing cortical inhibitory interneurons. J Neurosci 32:331–343.

Xue M, Atallah BV, Scanziani M (2014) Equalizing excitation-inhibition ratios across visual cortical neurons. Nature 511:596–600.

Zonouzi M, Berger D, Jokhi V, Kedaigle A, Lichtman J, Arlotta P (2019) Individual oligodendrocytes show bias for inhibitory axons in the neocortex. Cell Rep 27:2799–2808.e3.